Adv Biol (Weinh). Author manuscript; available in PMC 2021 June 01.

Published in final edited form as:
Adv Biol (Weinh). 2021 March 01; 5(3): e2000223. doi:10.1002/adbi.202000223.

Electrophysiological Phenotype Characterization of Human iPSC-Derived Neuronal Cell Lines by Means of High-Density Microelectrode Arrays

Silvia Ronchi, **Dr. Alessio Paolo Buccino**, **Gustavo Prack**, **Dr. Sreedhar Saseendran Kumar**, **Dr. Manuel Schröter**
Department of Biosystems Science and Engineering, ETH Zürich Mattenstrasse 26, Basel 4058, Switzerland

Dr. Michele Fiscella
Department of Biosystems Science and Engineering, ETH Zürich Mattenstrasse 26, Basel 4058, Switzerland

MaxWell Biosystems AG Albisriederstrasse 253, Zürich 8047, Switzerland

Andreas Hierlemann [Prof]
Department of Biosystems Science and Engineering, ETH Zürich Mattenstrasse 26, Basel 4058, Switzerland

Abstract

Recent advances in the field of cellular reprogramming have opened a route to studying the fundamental mechanisms underlying common neurological disorders. High-density microelectrode-arrays (HD-MEAs) provide unprecedented means to study neuronal physiology at different scales, ranging from network through single-neuron to subcellular features. In this work, HD-MEAs are used in vitro to characterize and compare human induced-pluripotent-stem-cell-derived dopaminergic and motor neurons, including isogenic neuronal lines modeling Parkinson's disease and amyotrophic lateral sclerosis. Reproducible electrophysiological network, single-cell and subcellular metrics, which are used for phenotype characterization and drug testing. Metrics, such as burst shape and axonal velocity, enable the distinction of healthy and diseased neurons. The HD-MEA metrics can also be used to detect the effects of dosing the drug retigabine to human motor neurons. Finally, it is shown that the ability to detect drug effects and the observed culture-to-culture variability critically depend on the number of available recording electrodes.

Correspondence to: Silvia Ronchi.Correspondence to: Michele Fiscella.
silvia.ronchi@bsse.ethz.ch; michele.fiscella@bsse.ethz.ch.

Conflict of Interest
The authors S.R., A.P.B., G.P, S.S.K., M.S., and A.H. declare no competing financial interests. M.F. is co-founder of MaxWell Biosystems AG, which commercializes HD-MEA technology.

Author Contributions
S.R. contributed to the work design, performed and planned the experiments, analyzed and interpreted data, wrote the manuscript. A.P.B contributed to spike sorting data and velocity computation. G.P. contributed to perform experiments and to velocity computation. S.S.K. contributed to statistical analysis. M.S. contributed to writing the manuscript. M.F. coordinated and conceived the project, contributed to work design and data interpretation, and wrote the manuscript. A.H. coordinated and conceived the project and contributed to writing the manuscript. All the authors have approved the submitted version and revised it.

Keywords

electrophysiology; high-density microelectrode arrays; induced pluripotent stem cells

1 Introduction

The advent of efficient cellular reprogramming protocols has revolutionized stem cell research and enabled access to a large variety of human cell lines.[1] Induced-pluripotent-stem-cell (iP SC)-technology has been used to establish 2D and 3D human cell and tissue models[2] and to study organ genesis for, e.g., liver,lungs,heart[5] and brain.[6] Today, iPSC technology allows to obtain cells and tissue samples from both, healthy individuals and patients and to develop in-vitro disease models.[7] Genetically-defined human iPSC-derived neurons have been generated to investigate physiological aspects and mechanisms underlying common neurological disorders[8] and for usage in in-vitro platforms for systematic drug testing.[9,10]

Functional phenotype characterization and drug-effect assessment of human neurons can be performed in vitro by using optical methods (e.g., calcium imaging[11]), patch-clamp techniques,[12] or by using microelectrode arrays (MEAs).[13] MEAs feature a set of metal electrodes to record electrical activity simultaneously from several hundreds to thousands of cells and have been used to study brain disorders and to detect differences between normal and pathological conditions.[14,15]

Passive MEA devices[16–18] without active circuit elements feature 10–100 electrodes per mm^2 and have been used to electrically characterize human neuronal phenotypes.[9,10,14] Complementary-metal-oxide-semiconductor (CMOS)-based high-density microelectrode arrays (HD-MEAs)[19–24] feature active circuit elements and electrode densities of tens to thousands of electrodes per mm^2 and have been used in first experiments to characterize electrical properties of healthy human iPSC-derived neurons.[25] However, to the best of our knowledge, CMOS-based HD-MEAs have not been yet used to comprehensively characterize and compare electrical phenotypes of human neuronal line across scales including network, single-neuron and subcellular features and to assess the effects of neurological disorders.

Among neurodegenerative disorders, Parkinson’s disease and amyotrophic lateral sclerosis have been extensively studied by using iPSC technology in order to understand basic disease mechanisms at molecular and functional levels and for finding new cures.[26–29]

Parkinson’s disease (PD) is among the most common neurodegenerative diseases, with a prevalence increasing from 2.5 million patients in 1990 to 6.1 million patients in 2016,[30] and projections indicating that more than 12 million people will be affected by 2050.[30] PD is characterized by the death of dopaminergic neurons within the substantia nigra, which causes progressive motor and cognitive dysfunctions, such as tremor, rigidity and dementia.[31] The distinctive hallmark of PD is the accumulation of intracellular α-synuclein, which forms protein inclusions, known as Lewy bodies and Lewy neurites.[31] Human iPSC-derived neurons modeling PD have been studied in vitro and showed compromised neuronal morphology,[32] synaptic connectivity[33] and different electrophysiological characteristics including, e.g., the shape of action potential waveforms.[34]

Amyotrophic lateral sclerosis (ALS) is a neurodegenerative disease, characterized by a progressive degeneration of upper and lower motor neurons, followed by muscle degeneration, paralysis, and respiratory failure.[35] ALS incidence is reported to be between 0.6 and 3.8 per 100 000 persons per year.[36] Human iPSC-derived neurons, developed to model ALS, featured an intrinsic membrane hyperexcitability phenotype,[10] which was used to test compounds that lowered neurons' electrical hyperexcitability. The study of Wainger et al., which relied on 64 microelectrodes, placed at a pitch of 200 μm in a 12-well platform, led to clinical testing of retigabine in human patients.[10]

Combining human iPSC-derived neurons with large-scale electrophysiological techniques, such as HD-MEAs, provides a powerful and scalable platform to study neurological disease mechanisms and offers the potential to assess disease-induced phenotypic alterations.

Here, we used CMOS-based high-density microelectrode arrays (HD-MEAs) to characterize and compare the electrical phenotypes of four iPSC-derived neuronal cell lines: human dopaminergic neurons (hDNs), dopaminergic neurons carrying the A53T α-synuclein mutation, linked to PD (hDNs-PD), motor neurons (hMNs), and motor neurons carrying the TDP-43 Q331K mutation, linked to ALS (hMNs-ALS). We found significant functional phenotype differences across the studied iPSC lines at different spatiotemporal scales, ranging from network level to characteristics of individual axons. We then used HD-MEA-based readouts to quantify the effect of the drug retigabine on motor neurons (hMNs)[10,37] and we showed that high-spatiotemporal-resolution sampling of neuronal activity by means of HD-MEAs provides very reproducible readouts in assessing the effects of neuroactive compounds.

2 Results

2.1 Human iPSC-Derived Neurons Develop Spontaneous Activity on HD-MEA Chips

Before probing the developing neurons and neuronal networks, we confirmed the presence of characteristic cell-type specific neuronal markers for each iPSC line. Human iPSC-derived and rat primary neuronal cultures, used for benchmarking, showed electrical activity across the entire HD-MEA chip electrode area (Figure 1a). The electrically active areas contained mature neurons as confirmed by microscope imaging of MAP2-positive cells (Figure 1b). The presence of astrocytes in the cell cultures was confirmed immunohistochemically by GFAP[38,39] and S100-β [39] staining (Figure 1c). An anti-GFAP antibody was used as a reactive astrocyte marker for rat primary cultures, which underwent the isolation procedure. An anti-S100-β antibody was used as astrocyte marker for human cell lines, as its efficiency was already demonstrated with human lines.[40] Furthermore, we visualized motor and dopaminergic neurons on the HD-MEA chips using the motor-neuron marker SMI-32[38] (Figure 1c, central panel) and the dopaminergic-neuron marker TH[41] (Figure 1c, right panel). Human and rat neurons were all electrically active and showed spontaneous action-potential signals, which systematically crossed the detection threshold (Figure 1d).

2.2 Electrical Phenotype Characterization of Human iPSC-Derived Neurons across Development

To compare the electrophysiological properties across the four human iPSC-derived neuronal cell lines, we first examined and compared the mean firing rate (MFR), mean spike amplitude (MSA), mean inter-spike interval (ISI) coefficient of variation (ISIcv) and the percentage of active electrodes (pAE). Changes in metrics as the firing rate are hallmarks of neuronal development,[10] but they can also be indicative of a specific neuron type[42] or pathology.[10] We also compared the iPSC-derived cell lines electrophysiological properties with the ones of rat primary cortical neurons (rPCNs), the most commonly used neuronal cells in the MEA field and an established in-vitro culturing system, across development (for details, see Figure S1). Both, motor (hMN) and dopaminergic (hDN) neuronal lines showed a significant increase (7 fold and 1.9 fold) in the mean firing rate from DIV 7 to DIV 21 (Figure 2a,b), similar to rPCNs (Figure S1c).

hMNs featured a higher mean firing rate, mean spike amplitude and percentage of active electrodes compared to hDNs (Figure 2b). In particular, at DIV 21, the hMN mean firing rate (1.98 ± 1.30 Hz) was 3.5 times higher ($p < 0.001$, Wilcoxon rank-sum test) than the hDN mean firing rate (0.57 ± 0.10 Hz). The hMN mean spike amplitude and percentage of active electrodes were 1.5-fold and 1.7-fold higher than that of the hDN line (Figure 2b). However, the mean ISI coefficient of variation did not vary significantly across development between hMNs and hDNs, which showed a similar behavior in neuron-firing-rate evolution over development. Both, hMNs and hDNs showed significantly lower mean spike amplitudes in comparison to rPCNs at DIV 21. rPCNs had an average mean spike amplitude of 95.01 ± 8.96 μV, whereas hMNs and hDNs featured mean spike amplitudes of 44.23 ± 14.62 μV and 29.17 ± 2.78 μV, respectively (Figure S1c and Figure 2b). Furthermore, the variation in the mean spike amplitude across development was less in hMNs and hDNs than that of rPCNs (Figure S1c and Figure 2b). Human iPSC-derived neuronal lines were also characterized by an almost constant ISI coefficient of variation across development, in contrast to the increase in rPCNs (Figure S1c and Figure 2b).

Comparing healthy (WT) and diseased (ALS) motor neuron lines, the hMN-ALS neuronal cells featured a 0.5-fold ($p < 0.05$) lower mean firing rate than hMNs at DIV 14 (Figure 2c). Similar results were found by comparing the two dopaminergic neuron lines, which showed a 0.8-fold ($p < 0.01$) lower mean firing rate of hDN-PDs in comparison to hDNs at DIV 21 (Figure 2d). Analysis of the mean spike amplitudes showed no significant differences between hMN and hMN-ALS neurons. In contrast, the two dopaminergic neuron lines, hDN and hDN-PD, showed significant differences in the mean spike amplitude at DIV 7 ($p < 0.05$) (Figure 2c).

The mean ISI coefficient of variation evidenced a more regular firing of the hMN line at DIV 7 in comparison to the hMN-ALS line (Figure 2c). Conversely, the disease line hDN-PD featured a more regular firing at DIV 21 in comparison to the healthy hDN line (Figure 2d).

Finally, by comparing the percentage of active electrodes across development, we did not find significant differences between hMN and hMN-ALS or hDN and hDN-PD lines;

however, pAE data generally were very disperse, suggesting that potential differences in MFR between cell types could also be a consequence of the ability of the specific cell line to form functional neuronal networks (Figure 2b–d).

2.3 Network Burst Characterization of Human iPSC-Derived Neurons across Development

Neuronal networks are often characterized by synchronous activity (bursts), which may give rise to network oscillations.[43] These bursts emerge as a result of recurrent synaptic connections that form as neuronal networks mature. In primary cortical neurons, the bursts are often irregular even in mature networks[44,45] (Figure S2). The nature and properties of the associated oscillations may vary for different pathological conditions[46] or in co-cultures with different cell types.[42]

Here, we assessed the characteristic properties of human healthy and diseased cell lines by using network-burst metrics including mean burst duration (BD), mean inter-burst interval (IBI), mean IBI coefficient of variation (IBIcv), number of bursts per minute ($B_{/\mathrm{min}}$) and burst shape (see the Experimental Section, HD-MEA Metrics).

All human iPSC-derived neuronal cultures showed robust and reproducible network oscillations at DIV 14 and 21 (Figure 3a, Figure S2). hMNs and hDNs featured significant differences in IBI, IBIcv and $B_{/\mathrm{min}}$ at both DIVs 14 and 21 (Figure 3b). hDNs featured a 2.4-fold increase ($p < 0.0001$, Wilcoxon rank-sum test) in time between consecutive bursts compared to hMNs at DIV 21 (Figure 3b). hDNs displayed more regular bursts than hMNs, which is shown by a 0.3-fold decrease ($p < 0.001$) in IBIcv between consecutive bursts at DIV 21 (Figure 3b). Furthermore, at DIV 21 hDNs showed in average 2.2-fold less bursts per minute ($p < 0.0001$) than hMNs (Figure 3b).

Comparing motor-neuron lines, we found that hMN-ALS neurons featured a longer burst duration of 16.56 ± 5.44 s than hMNs (3.91 ± 2.59 s) at DIV 21 (Figure 3c). Converse results were found for the healthy and isogenic diseased dopaminergic-neuron lines, where hDN-PDs showed a 0.5-fold decrease ($p < 0.0001$) of the burst duration at DIV 21 compared to hDNs (Figure 3d).

By comparing the inter-burst interval times of healthy and diseased lines at DIV 21, we found that the hMN-ALS line had a 3.2-fold longer IBI ($p < 0.0001$) than the healthy hMN line (Figure 3c), while the hDN-PD line showed a 0.6-fold shorter IBI ($p < 0.0001$) than the healthy hDN line (Figure 3d).

An analysis of the IBI coefficients of variation yielded no significant differences between hMN and hMN-ALS lines (Figure 3c). However, the dopaminergic neuron lines showed a small difference at DIV 21 ($p < 0.05$) (Figure 3d).

Comparing the number of bursts per minute recording ($B_{/\mathrm{min}}$) of healthy and diseased lines, we found that hMNs featured a 3-fold higher ($p < 0.0001$) number of bursts per minute than hMN-ALSs at DIV 21 (Figure 3c). Instead, hDNs featured a 0.62-fold lower ($p < 0.0001$) number of bursts per minute than the diseased line at DIV 21 (Figure 3d).

2.4 Network-Burst Shape Can be Used to Characterize Human iPSC-Derived Neuron Lines

By inspecting the population spike time histograms (Figure 4a), we noticed that each human iPSC-derived neuronal line featured a characteristic burst shape across every activity peak (see also Figure S2). Therefore, we assessed the ability to discriminate hMN and hMN-ALS or hDN and hDN-PD neurons by their network burst shape at a given day in vitro. For this purpose, we computed the linear correlations between every single recorded network burst and the corresponding network burst templates generated by averaging over many electrodes and HD-MEAs or wells harboring the same cell line at the specific DIV (see the Experimental Section, HD-MEA Metrics). In Figure 4b, we show the network burst template for hMNs at DIV 14 and DIV 21 (see the Experimental Section, HD-MEA Metrics). When we linearly correlated single recorded hMN bursts at DIV 14 to the DIV14 hMN template, we obtained an average Pearson Correlation Coefficient (PCC) of 0.97 ± 0.01, which indicated a high similarity between the burst template and the single bursts. However, upon correlating single DIV14 hMN-ALS bursts to the DIV14 hMN template, the average PCC decreased to 0.89 ± 0.06 (Figure 4b) and to 0.71 ± 0.12 for correlating DIV21 hMN-ALS bursts to the DIV21 hMN template (Figure 4b).

In Figure 4d, we used the network burst templates of hDNs at DIVs 14 and 21. The DIV 14 hDN template yielded an average Pearson Correlation Coefficient (PCC) of 0.98 ± 0.01 upon application to single hDN recorded bursts at DIV 14. Upon using the DIV14 hDN template for single hDN-PD bursts recorded at DIV 14, the average Pearson Coefficient decreased to 0.96 ± 0.03 ($p < 0.001$, Wilcoxon rank-sum test) (Figure 4d). At DIV 21, the application of the DIV21 hDN template for DIV21 hDN-PD bursts yielded a further decreased PCC of 0.89 ± 0.03 (Figure 4d).

In Figure 4c and 4e, the inverse correlations by using the hMN-ALS and hDN-PD disease line templates are shown. Expectedly, the correlations are stronger between the disease-line templates and the respective disease line bursts at both DIVs as compared to bursts of the healthy lines. As the disease lines featured a somewhat larger burst shape irregularity, the discrimination by using the disease line templates was less efficient in comparison to the healthy line templates.

2.5 Axonal Action Potential Propagation in Healthy and Diseased Human iPSC-Derived Neurons

The HD-MEA chip used in this work allows for reading out neuronal electrical activity at subcellular resolution.[47–49] Measurements of action potential propagation velocities and potential alterations can be used to functionally differentiate neuronal cell types,[50] to study axonal development[51,52] and to get indications of axon degeneration.[53] Here, exploiting the high spatiotemporal resolution of HD-MEAs, we determined action-potential propagation velocities by tracking the AP propagation in space and time simultaneously across multiple electrodes (Figure 5a–c and Figure S3). Action potentials are initiated at the AIS,[48] which produces the largest extracellular voltage signal,[48] and then propagate along the axon, while AP amplitudes decrease (Figure 5b).

To test if axonal-action-potential-propagation velocities differed between healthy and diseased cell lines, we estimated (see the Experimental Section, Action Potential Propagation Velocity) the respective velocities of healthy motor neurons and ALS motor neurons and over several DIVs (14, 28 and 42). Results showed differences in velocities during more mature stages, i.e., at DIV 42 (Figure 5d). At DIV 42, hMNs featured an average velocity of 480 ± 190 mm s^{-1}, while hMN-ALS neurons featured a significantly higher average axonal AP-propagation velocity of 560 ± 200 mm s^{-1} ($p < 0.01$, Wilcoxon rank-sum test).

The same measurements were conducted for healthy dopaminergic neurons and PD dopaminergic neurons. However, in contrast to motor neurons, healthy and diseased dopaminergic neurons did not show any significant difference in axonal propagation velocity (hDNs: 230 ± 80 mm s^{-1}, hDN-PDs: 280 ± 120 mm s^{-1} at DIV 42). The hDN lines featured comparably small signal amplitudes, which yielded less neurons that could be identified in the recordings. Although the spike sorting parameters were adjusted to also include neurons with smaller amplitudes (see the Experimental Section, Spike Sorting), only few hDN neurons satisfied the propagation-velocity conditions described in the Experimental Section (Action Potential Propagation Velocity) and could be used to assess axonal propagation speeds.

2.6 The Effects of Retigabine on Spontaneous Neuronal Activity at Network, Single-Cell, and Subcellular Levels

Retigabine is an anticonvulsant drug used for epilepsy treatment. It opens neuronal K(v) 7.2–7.5 (formerly KCNQ2-5) voltage activated K(+) channels that generate the M-current, a subthreshold K(+) current needed to stabilize the membrane potential and control neuronal excitability.[54] The effects of retigabine dosage have been analyzed by monitoring neuron spiking rates using a 64-electrode MEA, which were found to significantly decrease.[10,37,55] Moreover, retigabine was also reported to decrease spontaneous electrical activity in neuronal cortical cultures by decreasing the mean burst rate.[56] Here, we explored the effects of retigabine on the inter-burst interval and number of active electrodes in cultures of healthy motor neurons at DIV14 (Figure 6), at DIV 21 (Figure S4a) and of diseased motor neurons at DIV 14 (Figure S4b). Additionally, we investigated how the spiking rate estimation may be influenced by the number of readout electrodes.

An analysis over the entire HD-MEA electrode array showed a significant reduction in the fraction of active electrodes one minute after applying concentrations 5 μm ($p < 0.017$, Kruskal-Wallis test, followed by Dunn-Sidák multiple-comparison test) and 10 μm ($p < 0.001$) (Figure 6a,b).

Using simultaneously 1020 electrodes in the active regions, we assessed the number of spikes per min (see the Experimental Section, Drug Administration), which was reduced to 79 ± 7% upon applying a concentration of 1 μm, to 19 ± 9% upon applying concentrations of 5 μm ($p < 0.017$), and to 6 ± 4% using 10 μm ($p < 0.001$) (Figure 6f, left), compared to the baseline recordings without retigabine treatment. This activity reduction was expected, as retigabine hyperpolarizes the cell membrane by opening potassium channels.

We also determined the mean inter-burst intervals, which increased 3.5-fold upon administration of 5 μm of retigabine (Figure 6c,d). The inter-burst interval also increased upon applying 10 μm retigabine, albeit the effect was more difficult to assess, as some HD-MEAs did not record any burst over the whole recording duration of 5 min.

Although retigabine caused significant changes in network firing properties and network bursting, retigabine doses of 1 μm and 5 μm did not significantly change the velocity of the propagating action potentials along axons (Figure 6e). Retigabine could potentially have altered AP propagation velocity along axons, as KCNQ channels are also present on dendrites and axon.[57] A very small decrease in conduction velocity was reported after retigabine administration in rat sciatic nerves.[58,59]

We also studied the effects of retigabine dosage at a different day in vitro and conducted the same drug experiment on hMNs at DIV 21. Results are reported in Figure S4a. Dosage of 10 μm retigabine decreased the spikes per min to 30 ± 15% ($p < 0.017$) and the pAE to 42 ± 17% ($p < 0.001$). Despite a trend similar to the results at DIV 14, retigabine dosage had less effects on the measured metrics, and the data variation was higher.

Moreover, we tested if retigabine also decreased spontaneous electrical activity in the isogenic diseased line hMN-ALS at DIV14. Results are shown in Figure S4b. Dosage of 10 μm retigabine decreased the spikes per min to 12 ± 7% ($p < 0.001$) and the pAE to 17 ± 10% ($p < 0.001$). The overall decrease in spontaneous activity of the diseased cells, however, was lower than that observed with healthy hMNs.

In a next step, we tested the influence of the number and configuration of used electrodes on the obtained spiking and IBI. In addition to the standard configuration comprising the 1020 most active electrodes at a minimum pitch of 35 μm, we used configurations of 64 electrodes (grids of 8 × 8 electrodes at 200 μm pitch) and 16 electrodes (4 × 4 grid at 200 μm pitch), see also Figure S5a. By using the 64-electrode configuration, we found similar relative changes in spikes per min for concentrations of 5 μm ($p < 0.017$) and 10 μm ($p < 0.017$), however, we noticed an increased variation of this metric across different cultures, as the number of spikes became very low upon dosage of larger concentrations of retigabine and some electrode configurations could not detect any spike (Figure 6f, center). Using 16-electrode configurations, arranged in a 4 × 4 grid, we obtained significant differences just between the control sample and 10 μm retigabine dosage ($p < 0.017$) (Figure 6f, right), as the scattering of the measured values was comparably large. Also in this case, some electrode configurations could not detect spikes at higher drug concentrations. As can be expected, a larger number of recording electrodes or sampling points provides more reliable results.

To compare the variability in the measurement data and to see in how far local effects may influence the results, we applied 6 different configurations of 8 × 8 and 4 × 4 electrodes across 4 HD-MEAs for control and 1 μm concentration and 5 HD-MEAs for 5 μm and 10 μm concentrations (Figure S5b, S5c). For the metric spikes per min, we could confirm a higher well-to-well variability with respect to the configuration with 1020 electrodes (Figure S5b), while for the metric IBI, we could not find significant differences between vehicle control and any drug concentration for the 64-electrode and the 16-electrode configurations (Figure S5c).

3 Discussion and Conclusion

We presented an investigation of the electrical phenotypes of several human iPSC-derived neuronal cell lines using HD-MEAs. We showed that HD-MEA technology – despite the low signal amplitudes of the hiPSC-derived neurons of approx. 30 μV to 45 μV - enables a reliable discrimination of the electrical activity of different neuronal lines at different developmental stages and across several levels, ranging from whole-network activity levels to subcellular structures. As more and more human iPSC-derived neuronal lines become available,[60] the possibility to extract and compare a multiparametric set of physiological features across different functional levels will improve (i) the functional characterization of those neuronal lines in healthy and diseased states and (ii) the evaluation of drug effects upon administration in vitro.

As a first step, we characterized all cell lines by investigating metrics, such as mean firing rate (MFR), mean inter-spike interval (ISIcv), mean spike amplitude (MSA) and percentage of active electrodes (pAE) (Figure S1 and Figure 2). In a next step, we extracted features from network bursts of neuron cultures on MEAs, including burst structure, oscillatory behavior and synchronicity[61] (Figures 3 and 4). Finally, we characterized neuronal lines by investigating axonal propagation velocities (Figure 5). In contrast to passive MEA devices that feature fixed electrode configurations, CMOS-based HD-MEAs offer the possibility to extract all aforementioned metrics from several active regions within a culture.[23,62] This feature enabled a reliable distinction of rPCNs from hDNs and hMNs based on the MFR, ISIcv, MSA, and pAE. (Figure S1 and Figure 2). Electrophysiological differences between rat primary cultures and human cell lines, especially for their firing rate, can possibly be explained by (i) the different neuronal maturation status,[13] (ii) the different astrocyte maturation status,[63] or/and (iii) the different astrocyte concentration,[63] as has been reported by other authors.

As for healthy and diseased motor neurons, hyperexcitability was reported in iPSC-derived motor neurons harboring A4V SOD1 mutations[10] and C9ORF72 repeat expansions.[64] In studies with motor-neuron-like cell lines, transfected with mutant Q331K TDP-43, the authors found that the TDP-43 mutation increased the firing frequency of action potentials.[65,66] In our characterization of motor neuron electrical activity, we did not find a higher mean firing rate or mean spike amplitude in hMN-ALS neurons as compared to control hMNs (Figure 2). In contrast, we found that the hMN-ALS burst duration was 4.2-fold longer (16 sec) than that of control hMNs at DIV 21 (Figure 3).

As for healthy and diseased dopaminergic neurons, a higher network-bursting activity of A53T α-synuclein PD neurons, in comparison to a human control line, was reported by Zygogianni et al.,[67] while other studies of network properties of PD neurons with mutations in the LRRK2 gene found that diseased neurons lacked synchronous network bursting activity.[68] Here, we found an increased frequency in synchronized population bursting activity for PD neurons, which is in agreement with the findings of Zygogianni et al.[67] (Figure 3). Furthermore, we found that PD neurons featured shorter burst duration and more variable inter-burst intervals compared to healthy dopaminergic neurons (Figure 3), which, again, is in agreement with the findings of Zygogianni.[67]

Comparing the healthy and diseased lines by their AP propagation velocity, we found an increased axonal AP-conduction velocity in Q331K TDP-43 neurons (Figure 5), which could be correlated with altered axonal excitability properties reported in previous ALS studies.[69,70] Human motor-neuron lines feature larger AP spike amplitudes than dopaminergic-neuron lines, so that a more reliable extraction of axonal signals and differences in axonal propagation velocity between cell lines at different DIVs was possible. However, it is important to notice that the commercially available human iPSC-derived lines, used in this study, do not contain 100% motor neurons or 100% dopaminergic neurons (see the Experimental Section, Cell Lines) (Figure 1), so that caution is advised in the interpretation of the data. Moreover, it is important to mention that only one line of h-iPSC derived neurons was used in each study group and that donor-to-donor differences, somatic mutations and experimental conditions greatly affect the electrophysiological properties of h-iPSC-derived neurons.

For a reliable comparison of subcellular features of genetically defined cell lines it is necessary to make sure that only neurons of the specified genetic type are characterized, which can be achieved by using the following experimental techniques or combinations thereof: (1) purification of neuronal lines by FACS sorting and subsequent plating;[10] (2) activation and identification of genetically-defined neurons in a mixed population by expression of opto- and chemogenetic markers, driven by cell-type-specific promoters;[71] (3) identification of cell types by extraction and classification of extracellular AP waveform features.[72,73]

In a prototype drug dosage experiment, we evaluated the drug effects upon administration in vitro (Figure 6). We used retigabine, a potassium channel opener, which decreases neural activity. As expected, retigabine significantly decreased the percentage of active electrodes, the number of spikes per minute, and increased the inter-burst interval with increasing concentration (Figure 6). Experiments were performed at DIV 14, as cultures were stable and characterized by network synchronous activity. Additionally, we investigated the effect of retigabine at DIV 21 and recorded similar compound effects. However, retigabine dosage had less effects on the measured metrics at DIV 21, and the data variation was larger than at DIV 14.

We did not find significant changes in AP propagation velocity across axonal arbors upon increasing drug dose (Figure 6). Nevertheless, owing to the high spatial resolution of the HD-MEA, we could reliably monitor the same neurons and their axonal arbors before and after drug treatment, so that we propose to include this new metric in the assessment of compound effects. We found that the number and density of used electrodes strongly influence the nature and number of metrics that can be used to assess drug effects (Figure 6). In particular, the availability of a comparably large number of electrodes (1020 electrodes simultaneously) enabled to capture the dynamics of multiple neurons, which increases the reliability of extracted metrics, such as recorded spikes per min. Additionally, our results showed that the use of a large number of flexible recording sites entailed a significantly lower intra-culture and culture-to-culture fluctuation as compared to applying fixed electrode configurations. By selecting readout electrodes, we could target areas, where active neurons were located, while fixed-grid arrangements do not offer this possibility. However, the results reported on here cannot be used to directly conclude on the performance of commercially available MEAs featuring less electrodes, as the electrode size also plays a role (averaging effect, see, e.g., reference[74]), which was not taken into account here.

In conclusion, HD-MEA technology enables to conduct noninvasive assays and to extract highly reproducible metrics, such as mean firing rate, mean spike amplitude and burst shape, for studying disease mechanisms at a functional level for a multitude of human neuronal lines.[75] In addition, HD-MEA technology provides accurate readouts at single-cell and subcellular levels, which can be used as complementary metrics for assessment of drug effects in human neuronal cultures.[76]

4 Experimental Section

High-Density Microelectrode Arrays

CMOS-based HD-MEAs[23,62] were used to record the extracellular signals of human iPSC-derived and rat primary neurons. The HD-MEA features 26 400 electrodes organized in a 120 × 220 grid within a total sensing area of 3.85 × 2.10 mm^2. The electrode area is 9.3 × 5.45 μm^2, and the center-to-center electrode distance (pitch) is 17.5 μm, which allows for recording of cell electrical activity at subcellular resolution. A user-selected configuration of 1024 electrodes can be simultaneously recorded from (see also the Experimental Section, HD-MEA Recordings). The HD-MEA features noise values of 2.4 μV$_{rms}$ in the action potential band of 0.3 – 10 kHz and has a programmable gain of up to 78 dB. The sampling frequency is 20 kHz. We used the MaxOne HD-MEA produced by MaxWell Biosystems AG (www.mxwbio.com) and the laboratory version of the same HD-MEA,[62] which only differs in the design of the printed circuit board (PCB).

Cell Lines

Human iPSC-derived neurons and astrocytes (iCell® DopaNeurons, iCell® Motor Neurons, iCell® DopaNeurons A53T, iCell® Motor Neurons Q331K, iCell® Astrocytes) were purchased from FCDI (FUJIFILM Cellular Dynamics International, Madison, USA). We used two dopaminergic-neuron cell lines: a mixed population of healthy A9 and A10 subtype human dopaminergic neurons (hDNs), which have been demonstrated to express relevant midbrain dopamine neuronal markers (see also Figure 1), and an isogenic variant harboring the early-onset mutation A53T α-synuclein (hDN-PD) as a disease line. The A53T α-synuclein mutation renders α-synuclein susceptible to aggregation, which has been proposed as contributor to PD pathology.[77]

We used healthy human spinal motor neurons (hMNs) with expression of characteristic motor neuron markers (e.g., SMI-32), and an isogenic diseased motor neuron cell line carrying the TDP-43 Q331K mutation (hMN-ALS). Dominant mutations in the RNA/DNA-binding protein TDP-43 have been linked to amyotrophic lateral sclerosis (ALS).[78]

We used co-cultures of human motor neurons (hMN: 93% Tuj$^+$/Nes$^-$, 93% Isl1/2^{+1} at 14dPT by flow cytometry) and astrocytes (98% CD44$^+$/ S100β+, 74% GFAP$^+$, 2% Tau$^+$, by flow cytometry) and co-cultures of human dopaminergic neurons (hDN: 92% Map2$^+$/Nes, 81% FoxA2$^+$, 89% TH$^+$ by flow cytometry) and astrocytes at a ratio of 5:1. Astrocytes were added, as they support neuronal functioning in cultures, enhance the culture development[79] and mediate network synchronicity.[80] In particular, healthy astrocytes, co-cultured with healthy and diseased cell lines, help to achieve stable cultures and enable to correlate observed electrophysiological phenotypes to specific neuronal types.

Rat primary neurons were obtained from dissociated cortices of Wistar rats at embryonic day 18, using the protocol described in Ronchi et al., 2019.[81] All animal experimental protocols were approved by the Basel-Stadt veterinary office according to Swiss federal laws on animal welfare and were carried out in accordance with the approved guidelines.

Cell Plating

Prior to cell plating, HD-MEA chips were sterilized using 70% ethanol for 30 minutes. Ethanol was then removed, and the chips were rinsed three times with sterile tissue-culture-grade water. The HD-MEA chips were coated with chemicals to render the surface more hydrophilic. We adopted two different coating protocols suggested by the FCDI guidelines, depending on the cell type: for the motor-neuron plating, we treated the surface poly-D-lysine (PDL, 20 μL, 0.1 mg mL^{-1}) (A3890401, Gibco, ThermoFisher Scientific, Waltham, USA) for 1 hour at room temperature; for the dopaminergic-neuron plating, we used poly-L-ornithine (PLO, 20 μL, 0.05 mg mL^{-1}) solution (A-004-C, Sigma-Aldrich, St. Louis, USA) for 2 hours in a 5% CO_2 cell culture incubator at 37 °C. The PDL and PLO solutions were then aspirated, and the electrode surfaces were rinsed three times with sterile water.

On the plating day, extracellular-matrix-protein solutions were added to promote cell adhesion. Before plating the motor neurons, Geltrex extracellular-matrix solution (10 μL, 0.16 mg mL^{-1}) (A1569601, Gibco) was pipetted onto the array and left for 1 hour at room temperature. Before plating the dopaminergic neurons, Laminin solution (10 μL, 80 μg mL^{-1}) (L2020-1MG, Sigma-Aldrich) was pipetted onto the array for 30 minutes at 37 °C.

Frozen neuron and astrocyte vials were thawed for 3 minutes at 37 °C in a water bath, thereafter, 7 mL of medium was added to dilute the dimethyl sulfoxide (DMSO). The vials were then centrifuged for 5 minutes at 1600 rpm. Neurons and astrocytes were resuspended in medium to the desired ratio of 100 000 neurons and 20 000 astrocytes and then plated onto the HD-MEA chips in a 10 μL medium drop. The cells on the HD-MEA chips were incubated in a 5% CO_2 cell-culture incubator at 37°C for 1 hour. After cell adherence to the HD-MEA-chip surface, each well was filled with 0.6 mL of maintenance medium (see below). A 50% medium exchange was performed one day after plating, followed by 33% medium exchanges twice a week.

Maintenance medium consisted of Brainphys (0 5790, STEMCELL Technologies, Vancouver, Canada), supplemented with 2% iCell neural supplement (type B for dopaminergic neurons, type A for motor neurons) (FCDI), 1% iCell nervous-system supplement (FCDI), 1% of 100X *N*-2 supplement (17 502 048, Gibco), 0.1% laminin (L2020-1MG, Sigma-Aldrich) and 1% of 100X penicillin-streptomycin (15 140 122, Gibco).

During the first week in vitro, motor-neuron medium was supplemented with 5 µm DAPT (D5942, Sigma-Aldrich) to prevent outgrowth of proliferative cells.

E18 rat primary cortical neurons were isolated, plated and maintained according to protocols described previously.[81]

HD-MEA Recordings

Recordings were performed weekly, starting from DIV 7. The recording setup was placed inside a 5% CO_2 cellculture incubator at 37 °C, which entailed a stable pH-value of the cell culture medium. We used the “Activity Scan Assay” and “Network Assay” modules, featured in the MaxLab Live software (MaxWell Biosystems AG, Zurich, Switzerland), to monitor and record neuronal electrical activity. Seven electrode configurations, including a total of 6600 electrodes at a pitch of 35 µm (every second electrode in x and y), were used to map spontaneous neuronal electrical activity across the entire HD-MEA chip. Each electrode configuration was recorded during 120 seconds (“Activity Scan Assay”). After scanning the entire HD-MEA, we selected 1024 electrodes from the identified active electrodes and recorded network electrical activity for 300 seconds (“Network Assay”). Active electrodes were identified based on their firing rate, and among those the 1024 electrodes featuring the highest firing rates were selected. The number of used HD-MEAs per condition (N) is always indicated in the figures in the Results section.

Data Analysis

Data analysis was performed using custom-written codes in MATLAB R2019a and Python 3.6.10.

HD-MEA Metrics

To characterize and compare the neuronal cultures, we used two categories of metrics: electrode metrics and well metrics. Metrics were first computed at electrode level. Then, the electrode metrics were averaged to represent a single HD-MEA chip or well. A spike was defined as a negative voltage deflection, whose amplitude exceeded 5 times the standard deviation of the baseline noise. Metrics indicated with asterisks (*) were adapted from Tukker et al., 2018[42] and Cotterill et al., 2016.[45] The following parameters and metrics were used to assess neuronal characteristics.

1. Electrode firing rate (eFR) was defined as the number of spikes n_i^{sp} observed in a pre-defined time interval T, recorded on a single electrode i:

$$\mathrm{eFR}_i = \frac{n_i^{sp}}{T} \tag{1}$$

2. Well mean firing rate* (MFR) was defined as the mean of the eFR computed over the most active (electrodes with highest eFR) 1024 electrodes ($N = 1024$), simultaneously recorded:

$$\mathrm{MFR} = \frac{1}{N}\sum_{i=1}^{N} \mathrm{eFR}_i \tag{2}$$

3. Electrode spike amplitude (eSA) was defined as the 90th percentile of the recorded spike amplitudes on a single electrode i:

$$\mathrm{eSA}_i = \frac{90}{100} \times \mathrm{M}_i \tag{3}$$

   where M_i is the length of the corresponding spike-amplitude vector, with amplitudes sorted from the smallest to the largest value.

4. Well mean spike amplitude (MSA) was defined as the mean of the eSA, computed over the most active 1024 electrodes ($N = 1024$), simultaneously recorded:

$$\mathrm{MSA} = \frac{1}{N}\sum_{i=1}^{N} \mathrm{eSA}_i \tag{4}$$

5. Electrode inter-spike interval coefficient of variation (eISIcv) was defined as the inter-spike interval (ISI) standard deviation, divided by the ISI mean (μISI), where the ISI is the time difference between two consecutive spikes times tj, recorded on a single electrode i:

$$\mu\mathrm{ISI}_i = \frac{1}{N_{sp} - 1}\sum_{j=1}^{N_{sp} - 1}\left(t_{j+1} - t_j\right) \tag{5}$$

$$eISIcv_i = \frac{\sqrt{\frac{1}{N_{\mathrm{sp}} - 1} \times \sum_{j=1}^{N_{\mathrm{sp}} - 1} \left|\left(t_{j+1} - t_j\right) - \mu\mathrm{ISI}_i\right|^2}}{\mu\mathrm{ISI}_i} \tag{6}$$

6. Well inter-spike interval coefficient of variation* (ISIcv) was defined as the mean of the eISIcv, computed over the most active 1024 electrodes ($N = 1024$), simultaneously recorded:

$$\mathrm{ISl}cv = \frac{1}{N}\sum_{i=1}^{N} \mathrm{elSl}cv_i \tag{7}$$

7. Well percentage of active electrodes (pAE) was defined as the percentage of electrodes with eFR > 0.1 Hz and eSA < −15 μV, per well. All electrode metrics described above (1-6) and all well metrics described below (8-11) were only

computed for electrodes satisfying these two conditions for active electrodes (eFR > 0.1 Hz and eSA < −15 μV).

8. Well mean burst duration* (BD) was defined as the average duration of the network oscillations (bursts), recorded in a well:

$$\mathrm{BD} = \frac{1}{N_\mathrm{b}} \sum_{k=1}^{N_\mathrm{b}} \left(t_{e,k} - t_{\mathrm{s},k}\right) \tag{8}$$

where N_b is the number of bursts, t_e represents the burst end point and t_s the burst starting point as illustrated in Figure S6. The fast Fourier transform (FFT) was used to compute the main oscillation frequency and to correct for false positives as a consequence of high oscillation frequencies within each burst.

9. Well mean inter-burst interval* (IBI) was defined as the average time between the starting points of consecutive network bursts per well:

$$\mathrm{IBI} = \frac{1}{N_\mathrm{b} - 1} \sum_{k=1}^{N_\mathrm{b}-1} \left(t_{\mathrm{s},k+1} - t_{s,k}\right) \tag{9}$$

10. Well mean inter-burst interval coefficient of variation* (IBIcv) was defined as the inter-burst interval standard deviation, divided by the inter-burst interval mean (IBI) per well:

$$\mathrm{IBI}cv = \frac{\sqrt{\frac{1}{N_\mathrm{b}-1} \times \sum_{k=1}^{N_\mathrm{b}-1} \left|\left(t_{s,k+1} - t_{s,k}\right) - \mathrm{IBI}\right|^2}}{\mathrm{IBI}} \tag{10}$$

11. Well bursts per min* (B per min) was defined as the average number of bursts per one-minute time interval:

$$B_{/\mathrm{min}} = \frac{N_b}{t_m} \tag{11}$$

where tm represents the total recording time in minutes.

12. Well Pearson correlation coefficient (PCC) was defined as the average linear correlation between the network bursts of a well and a network burst template representing a specific cell type:

$$\mathrm{PCC}_k = \frac{1}{N_q - 1} \sum_{q=1}^{N_q} \left(\frac{b_q - \mu_b}{\sigma_b}\right)\left(\frac{temp_q - \mu_\mathrm{temp}}{\sigma_\mathrm{temp}}\right) \tag{12}$$

$$\mathrm{PCC} = \frac{1}{N_b - 1} \sum_{k=1}^{N_b-1} \mathrm{PCC}_k \tag{13}$$

where PCC_k represents the PCC between a single burst b (of mean μ_b and standard deviation σ_b) and a template *temp*, N_q the number of observations in the burst and PCC the mean of all PCC_k values computed in a specific well.

To characterize cell types according to their burst shape, eight templates were created, covering all cell types (hMN, hMN-ALS, hDN, hDN-PD) and each recorded DIV (14 and 21). The templates (temp) were obtained by averaging all recorded bursts in a well (temp_w and across wells of the same cell type and DIV:[82]

$$temp_w = \frac{1}{N_b}\sum_{k=1}^{N_b} b_k,\ \mathrm{temp}\ = \frac{1}{N_w}\sum_{w=1}^{N_\mu} temp_w \tag{14}$$

where N_b is the number of bursts per well, b_k denotes a single burst in a well, and N_w is the total number of wells featuring a specific cell type and DIV.

Spike Sorting

Spike sorting was performed to identify single units in the extracellular recordings. We ran spike sorting on the recordings, with which we covered the entire chip area (“Activity Scan Assay”) by using seven configurations of 960 electrodes (35 µm electrode pitch). We used the Kilosort2[83] software within the SpikeInterface[84] framework and the corresponding default parameters. Due to the large number of recordings, we automatically curated the spike sorting output according to the following criteria: for motor neurons, we removed clusters with less than 100 spikes, an ISI violation rate[85] above 0.3, and a signal-to-noise ratio (SNR) below 5; for dopaminergic neurons featuring less activity and lower signal amplitudes (Figure 3b), we removed clusters with less than 50 spikes and an SNR below 3 (the threshold on ISI violation rate was the same). Automatic curation was performed using the SpikeInterface package.[84]

Action Potential Propagation Velocity

Spike sorted and curated units were used to estimate the propagation velocity of action potentials. We discarded units with a small spatial extension template (averaged extracellular waveforms), and only kept units whose template covered at least 10 electrodes with an amplitude of more 10% of the maximum amplitude of the given unit. With these templates, we used a graphbased approach to find distinct neuronal branches. For each template, we considered the electrodes featuring a signal with an amplitude of at least 5% of the maximum amplitude and with a kurtosis value above 0.3 to filter out channels without a distinct signal peak. We then sorted the selected electrodes according to the time difference of the signal peak occurrence on that electrode with respect to the signal peak occurrence on the electrode showing the maximum signal amplitude, which most likely was close to the axon initial segment.[48] We then built a graph with the selected electrodes as nodes (Figure S7). Starting from the nodes with latest peak occurrence times (largest time difference),[86] each node was connected with edges to the three nearest electrodes with an earlier peak time. These three electrodes then formed the next set of nodes from which the procedure continued. Once the graph with all edges and nodes was built, we looked for the shortest paths along the nodes from each node to the electrode where the initial signal occurred, again starting from the electrodes with latest peak times or largest time differences. If an electrode formed already part of a path, it could not be used for another path. Finally, we removed duplicate paths by discarding the paths, where 50% of the nodes were in close proximity (<50 μm) to nodes of other paths. For the selected branches, distances were computed as the cumulative distance of all nodes between the initial electrode and the end of the path, while the peak times at the nodes included the differences between the peak time at the respective electrode and that at the initial electrode. Velocities were then estimated using a linear regression on the peak time differences and cumulative distances. We discarded branches with an $r^2 < 0.9$, and in cases that the algorithm found more than one branch for a template, we kept only the one with the highest r^2.

Statistical Analysis

Statistical comparisons between two populations were performed by using the non-parametric Wilcoxon rank sum test. Given two populations, the null hypothesis states that for randomly selected values A and B, drawn from each population, the probability of A being larger than B is equal to the probability of B being larger than A. To compare samples from more than two populations, we used the Kruskal-Wallis H test. Its null hypothesis is that the distribution of the dependent variables is the same across the considered populations. In case the null hypothesis was rejected, we performed a post-hoc Dunn test with Sidák correction for multiple comparisons (Dunn-Sidák multiple-comparison test).

Statistical analysis was performed in MATLAB R2019a. Sample sizes and data presentation methods are indicated in the legends of each figure.

Drug Administration

Retigabine (90 221, Sigma-Aldrich), dissolved in DMSO (D2650, Sigma-Aldrich) was applied at concentrations of 1 μm, 5 μm and 10 μm to a co-culture of healthy human motor neurons and astrocytes, similar to the experimental procedures reported by Wainger et al., 2014.[10] The vehicle control consisted of culture medium and DMSO (D2650, Sigma-Aldrich).

We performed recordings of motor neurons on each HD-MEA immediately before retigabine administration. We then conducted measurements one minute after drug administration. Data recorded after drug administration were normalized to data recorded before drug administration as $(\text{Parameter}_{\text{exposure}}/\text{Parameter}_{\text{baseline}}) \times 100$.[87] Hereafter, the ratio was normalized in reference to the values obtained with vehicle control.[87]

Drug effects were quantified about one minute after dosage by using the following metrics: spikes per min ($S_{/\text{min}}$), percentage of active electrodes (pAE) and mean inter-burst intervals (IBIs) (see the Experimental Section, HD-MEA Metrics).

The metric spikes per min (Figure 6b) for 1024, 64 and 16 electrodes was computed as:

$$S_{/\text{min}} = \frac{n^{\text{sp}}}{t} \tag{15}$$

Where n^{sp} is the total number of spikes recorded from all the recording electrodes during the recording time t in minutes. The resulting metric value, obtained from a drug-treated HD-MEA chip, was then normalized to the corresponding metric value, obtained from an untreated HD-MEA chip, in order to obtain a relative metric change (percent change) induced by the addition of the compound.

Microscopy and Staining

Neurons on HD-MEAs were fixed using a 4% paraformaldehyde solution (FB001, ThermoFisher Scientific). Fixation prevented cell necrosis and autolysis and preserved the cellular constituents. Samples were then permeabilized and blocked using a BPS 10 × (AM9625, ThermoFisher Scientific) solution containing 10% normal donkey serum (NDS) (017-000-001, Jackson ImmunoResearch, West Grove, USA), 1% bovine serum albumin (BSA) (0 5482, Sigma-Aldrich), 0.02% Na-Az (S2002, Sigma-Aldrich) and 0.5% Triton X (93 443, Sigma-Aldrich). Permeabilization facilitated antigen access to the cell, while blocking prevented non-specific binding of antibodies to the tissue. Primary and secondary antibodies were diluted in a PBS solution containing 3% NDS, 1% bovine serum albumin (BSA), 0.02% Na-Az and 0.5% Triton X.[81] The used antibodies are listed in Table 1.

We imaged cells on the HD-MEA chip with a Nikon NiE upright confocal microscope, with a Yokogawa W1 spinning-disk scan head.

Supplementary Material

Refer to Web version on PubMed Central for supplementary material.

Acknowledgements

M.F. and A.H. contributed equally to this work. This work was supported by the European Community through the European Research Council Advanced Grant 694829 “neuroXscales” and the corresponding proof-of-concept Grant 875609 “HD-Neu-Screen,” the Swiss Project CTI-No. 25933.2 PFLS-LS “Multi-well electrophysiology platform for high-throughput cell-based assays”, and through the Swiss National Science Foundation under contract 205320_188910/1. This work was also supported by an ETH Zürich Postdoctoral Fellowship 19-2 FEL-17 to A.P.B. The funders had no role in study design, data collection and analysis, decision to publish, or manuscript preparation. The authors thank Peter Rimpf and Tomislav Rebac for post-processing CMOS-based HD-MEAs. The authors thank the BEL group at ETH Zürich for valuable scientific discussions throughout the project. The authors thank Dr. Urs Frey, Dr. Marie Obien, and Dr. David Jäckel at MaxWell Biosystems for their contributions to data analysis and interpretation. The authors thank Dr. Xinyue Yuan (ETH Zürich) for input to the axon-propagation-velocity computation. The authors thank Dr. Vishalini Emmenegger (ETH Zürich) and Giulio Zorzi (MaxWell Biosystems) for the support with experimental design and execution. The authors thank Sam Malkin for proofreading the manuscript.

References

[1]. Takahashi K, Yamanaka S. Cell. 2006; 126:663. [PubMed: 16904174]
[2]. Liu C, Oikonomopoulos A, Sayed N, Wu JC. Development. 2018; 145
[3]. Si-Tayeb K, Noto FK, Nagaoka M, Li J, Battle MA, Duris C, North PE, Dalton S, Duncan SA. Hepatology. 2010; 51:297. [PubMed: 19998274]
[4]. Mou H, Zhao R, Sherwood R, Ahfeldt T, Lapey A, Wain J, Sicilian L, Izvolsky K, Lau FH, Musunuru K, Cowan C, et al. Cell Stem Cell. 2012; 10:385. [PubMed: 22482504]
[5]. Zhu W-Z, Van Biber B, Laflamme MA. Methods Mol Biol. 2011; 767:419. [PubMed: 21822893]

[6]. Theka I, Caiazzo M, Dvoretskova E, Leo D, Ungaro F, Curreli S, Managò F, Dell'Anno MT, Pezzoli G, Gainetdinov RR, Dityatev A, et al. Stem Cells Transl Med. 2013; 2:473. [PubMed: 23658252]

[7]. Park I-H, Arora N, Huo H, Maherali N, Ahfeldt T, Shimamura A, Lensch MW, Cowan C, Hochedlinger K, Daley GQ. Cell. 2008; 134:877. [PubMed: 18691744]

[8]. Dimos JT, Rodolfa KT, Niakan KK, Weisenthal LM, Mitsumoto H, Chung W, Croft GF, Saphier G, Leibel R, Goland R, Wichterle H, et al. Science. 2008; 321:1218. [PubMed: 18669821]

[9]. Laperle AH, Sances S, Yucer N, Dardov VJ, Garcia VJ, Ho R, Fulton AN, Jones MR, Roxas KM, Avalos P, West D, et al. Nat Med. 2020; 26:289. [PubMed: 31988461]

[10]. Wainger BJ, Kiskinis E, Mellin C, Wiskow O, Han SSW, Sandoe J, Perez NP, Williams LA, Lee S, Boulting G, Berry JD, et al. Cell Rep. 2014; 7:1. [PubMed: 24703839]

[11]. Schwab AJ, Ebert AD. Stem Cell Rep. 2015; 5:1039.

[12]. Bardy C, van den Hurk M, Kakaradov B, Erwin JA, Jaeger BN, Hernandez RV, Eames T, Paucar AA, Gorris M, Marchand C, Jappelli R, et al. Mol Psychiatry. 2016; 21:1573. [PubMed: 27698428]

[13]. Odawara A, Katoh H, Matsuda N, Suzuki I. Sci Rep. 2016; 6

[14]. Flaherty E, Zhu S, Barretto N, Cheng E, Deans PJM, Fernando MB, Schrode N, Francoeur N, Antoine A, Alganem K, Halpern M, et al. Nat Genet. 2019; 51:1679. [PubMed: 31784728]

[15]. Woodard CM, Campos BA, Kuo S-H, Nirenberg MJ, Nestor MW, Zimmer M, Mosharov EV, Sulzer D, Zhou H, Paull D, Clark L, et al. Cell Rep. 2014; 9:1173. [PubMed: 25456120]

[16]. Pine J. J Neurosci Methods. 1980; 2:19. [PubMed: 7329089]

[17]. Thomas C JR, Springer P, Loeb G, Berwaldnetter Y, Okun L. Exp Cell Res. 1972; 74:61. [PubMed: 4672477]

[18]. Gross GW, Rieske E, Kreutzberg GW, Meyer A. Neurosci Lett. 1977; 6:101. [PubMed: 19605037]

[19]. Eversmann B, Jenkner M, Hofmann F, Paulus C, Brederlow R, Holzapfl B, Fromherz P, Merz M, Brenner M, Schreiter M, Gabl R, et al. IEEE J Solid-State Circuits. 2003; 38:2306.

[20]. Berdondini L, Imfeld K, Maccione A, Tedesco M, Neukom S, Koudelka-Hep M, Martinoia S. Lab Chip. 2009; 9:2644. [PubMed: 19704979]

[21]. Bertotti, G, Velychko, D, Dodel, N, Keil, S, Wolansky, D, Tillak, B, Schreiter, M, Grall, A, Jesinger, P, Rohler, S, Eickenscheidt, M. , et al. 2014 IEEE Biomedical Circuits and Systems Conf Proc. IEEE; Lausanne, Switzerland: 2014. 304–307.

[22]. Frey U, Sedivy J, Heer F, Pedron R, Ballini M, Mueller J, Bakkum D, Hafizovic S, Faraci FD, Greve F, Kirstein KU, et al. IEEE J Solid-State Circuits. 2010; 45:467.

[23]. Ballini M, Muller J, Livi P, Chen Y, Frey U, Stettler A, Shadmani A, Viswam V, Jones IL, Jackel D, Radivojevic M, et al. IEEE J Solid-State Circuits. 2014; 49:2705. [PubMed: 28502989]

[24]. Viswam, V, Dragas, J, Shadmani, A, Chen, Y, Stettler, A, Muller, J, Hierlemann, A. IEEE Int Solid-State Circuits Conf. IEEE; San Francisco, CA, USA: 2016. 394

[25]. Amin H, Maccione A, Marinaro F, Zordan S, Nieus T, Berdondini L. Front Neurosci. 2016; 10:121. [PubMed: 27065786]

[26]. Okano H, Yasuda D, Fujimori K, Morimoto S, Takahashi S. Trends Pharmacol Sci. 2020; 41:99. [PubMed: 31926602]

[27]. Fujimori K, Ishikawa M, Otomo A, Atsuta N, Nakamura R, Akiyama T, Hadano S, Aoki M, Saya H, Sobue G, Okano H. Nat Med. 2018; 24:1579. [PubMed: 30127392]

[28]. Imamura K, Izumi Y, Watanabe A, Tsukita K, Woltjen K, Yamamoto T, Hotta A, Kondo T, Kitaoka S, Ohta A, Tanaka A, et al. Sci Transl Med. 2017; 9:eaaf3962. [PubMed: 28539470]

[29]. Benkert J, Hess S, Roy S, Beccano-Kelly D, Wiederspohn N, Duda J, Simons C, Patil K, Gaifullina A, Mannal N, Dragicevic E, et al. Nat Commun. 2019; 10

[30]. Rocca WA. Lancet Neurol. 2018; 17:928. [PubMed: 30287052]

[31]. Poewe W, Seppi K, Tanner CM, Halliday GM, Brundin P, Volkmann J, Schrag A-E, Lang AE. Nat Rev Dis Primers. 2017; 3

[32]. Prots I, Grosch J, Brazdis R-M, Simmnacher K, Veber V, Havlicek S, Hannappel C, Krach F, Krumbiegel M, Schütz O, Reis A, Wrasidlo W, et al. Proc Natl Acad Sci USA. 2018; 115:7813. [PubMed: 29991596]

[33]. Kouroupi G, Taoufik E, Vlachos IS, Tsioras K, Antoniou N, Papastefanaki F, Chroni-Tzartou D, Wrasidlo W, Bohl D, Stellas D, Politis PK, et al. Proc Natl Acad Sci USA. 2017; 114:3679.

[34]. Oliveira LMA, Falomir-Lockhart LJ, Botelho MG, Lin K-H, Wales P, Koch JC, Gerhardt E, Taschenberger H, Outeiro TF, Lingor P, Schüle B, et al. Cell Death Dis. 2015; 6:1994.

[35]. Mejzini R, Flynn LL, Pitout IL, Fletcher S, Wilton SD, Akkari PA. Front Neurosci. 2019; doi: 10.3389/fnins.2019.01310

[36]. Longinetti E, Fang F. Curr Opin Neurol. 2019; 32:771. [PubMed: 31361627]

[37]. Lombardo J, Harrington MA. J Neurophysiol. 2016; 116:2114. [PubMed: 27512022]

[38]. Egawa N, Kitaoka S, Tsukita K, Naitoh M, Takahashi K, Yamamoto T, Adachi F, Kondo T, Okita K, Asaka I, Aoi T, et al. Sci Transl Med. 2012; 4

[39]. Zhang Z, Ma Z, Zou W, Guo H, Liu M, Ma Y, Zhang L. Biomed Res Int. 2019; 2019

[40]. Hyvärinen T, Hyysalo A, Kapucu FE, Aarnos L, Vinogradov A, Eglen SJ, Ylä-Outinen L, Narkilahti S. Sci Rep. 2019; 9

[41]. Hallett PJ, Deleidi M, Astradsson A, Smith GA, Cooper O, Osborn TM, Sundberg M, Moore MA, Perez-Torres E, Brownell A-L, Schumacher JM, et al. Cell Stem Cell. 2015; 16:269. [PubMed: 25732245]

[42]. Tukker AM, Wijnolts FMJ, de Groot A, Westerink RHS. Neurotoxicology. 2018; 67:215. [PubMed: 29909083]

[43]. Bakkum DJ, Radivojevic M, Frey U, Franke F, Hierlemann A, Takahashi H. Front Comput Neurosci. 2014; 7:193. [PubMed: 24567714]

[44]. Chiappalone M, Bove M, Vato A, Tedesco M, Martinoia S. Brain Res. 2006; 1093:41. [PubMed: 16712817]

[45]. Cotterill E, Hall D, Wallace K, Mundy WR, Eglen SJ, Shafer TJ. J Biomol Screening. 2016; 21:510.

[46]. Görtz P, Siebler M, Ihl R, Henning U, Luckhaus C, Supprian T, Lange-Asschenfeldt C. Biochem Biophys Res Commun. 2013; 434:293. [PubMed: 23541573]

[47]. Bakkum DJ, Frey U, Radivojevic M, Russell TL, Müller J, Fiscella M, Takahashi H, Hierlemann A. Nat Commun. 2013; 4

[48]. Bakkum DJ, Obien MEJ, Radivojevic M, Jäckel D, Frey U, Takahashi H, Hierlemann A. Adv Biosyst. 2019; 3

[49]. Radivojevic M, Franke F, Altermatt M, Müller J, Hierlemann A, Bakkum DJ. Elife. 2017; 6:e30198. [PubMed: 28990925]

[50]. Sharma AD, McCoy L, Jacobs E, Willey H, Behn JQ, Nguyen H, Bolon B, Curley JL, Moore MJ. Sci Rep. 2019; 9

[51]. Dworak BJ, Wheeler BC. Lab Chip. 2009; 9:404. [PubMed: 19156289]

[52]. Shimba K, Sakai K, Isomura T, Kotani K, Jimbo Y. Integr Biol. 2015; 7:64.

[53]. Campanari M-L, Bourefis A-R, Kabashi E. Front Neurol. 2019:68. [PubMed: 30787905]

[54]. Blackburn-Munro G, Dalby-Brown W, Mirza NR, Mikkelsen JD, Blackburn-Munro RE. CNS Drug Rev. 2006; 11:1.

[55]. Moakley D, Koh J, Pereira JD, DuBreuil DM, Devlin A-C, Berezovski E, Zhu K, Wainger BJ. Sci Rep. 2019; 9

[56]. Wu C, Gopal KV, Lukas TJ, Gross GW, Moore EJ. EurJ Pharmacol. 2014; 732:68. [PubMed: 24681057]

[57]. Gunthorpe MJ, Large CH, Sankar R. Epilepsia. 2012; 53:412. [PubMed: 22220513]

[58]. Devaux JJ. J Neurosci. 2004; 24:1236. [PubMed: 14762142]

[59]. Roza C, Lopez-Garcia JA. Pain. 2008; 138:537. [PubMed: 18331780]

[60]. Avior Y, Sagi I, Benvenisty N. Nat Rev Mol Cell Biol. 2016; 17:170. [PubMed: 26818440]

[61]. Bader BM, Steder A, Klein AB, Frølund B, Schroeder OHU, Jensen AA. PLoS One. 2017; 12

[62]. Müller J, Ballini M, Livi P, Chen Y, Radivojevic M, Shadmani A, Viswam V, Jones IL, Fiscella M, Diggelmann R, Stettler A, et al. Lab Chip. 2015; 15:2767. [PubMed: 25973786]

[63]. Taga A, Dastgheyb R, Habela C, Joseph J, Richard J, Gross SK, Lauria G, Lee G, Haughey N, Maragakis NJ. Stem Cells Transl Med. 2019; 8:1272. [PubMed: 31631575]

[64]. Devlin A-C, Burr K, Borooah S, Foster JD, Cleary EM, Geti I, Vallier L, Shaw CE, Chandran S, Miles GB. Nat Commun. 2015; 6

[65]. Dong H, Xu L, Wu L, Wang X, Duan W, Li H, Li C. Neuroscience. 2014; 272:141. [PubMed: 24785678]

[66]. Buratti E. Adv Genet. 2015; 91:1. [PubMed: 26410029]

[67]. Zygogianni O, Antoniou N, Kalomoiri M, Kouroupi G, Taoufik E, Matsas R. Neurochem Res. 2019; 44:1475. [PubMed: 30989481]

[68]. Lin L, Göke J, Cukuroglu E, Dranias MR, VanDongen AMJ, Stanton LW. Cell Rep. 2016; 15:2411. [PubMed: 27264186]

[69]. Kanai K, Kuwabara S, Misawa S, Tamura N, Ogawara K, Nakata M, Sawai S, Hattori T, Bostock H. Brain. 2006; 129:953. [PubMed: 16467388]

[70]. Vucic S, Kiernan MC. Clin Neurophysiol. 2006; 117:1458. [PubMed: 16759905]

[71]. Berglund K, Tung JK, Higashikubo B, Gross RE, Moore CI, Hochgeschwender U. Methods Mol Biol. 2016; 1408:207. [PubMed: 26965125]

[72]. Weir K, Blanquie O, Kilb W, Luhmann HJ, Sinning A. Front Cell Neurosci. 2015; 8:460. [PubMed: 25642167]

[73]. Buccino AP, Kordovan M, Ness TV, Merkt B, Häfliger PD, Fyhn M, Cauwenberghs G, Rotter S, Einevoll GT. J Neurophysiol. 2018; :1212.120 [PubMed: 29847231]

[74]. Viswam V, Obien MEJ, Franke F, Frey U, Hierlemann A. Front Neurosci. 2019; 13:385. [PubMed: 31105515]

[75]. Huang C-Y, Liu C-L, Ting C-Y, Chiu Y-T, Cheng Y-C, Nicholson MW, Hsieh PCH. J Biomed Sci. 2019; 26:87. [PubMed: 31660969]

[76]. Kramer L, Nguyen HT, Jacobs E, McCoy L, Curley JL, Sharma AD, Moore MJ. ALTEX. 2020; 373:350.

[77]. Giasson BI, Duda JE, Quinn SM, Zhang B, Trojanowski JQ, Lee VM-Y. Neuron. 2002; 34:521. [PubMed: 12062037]

[78]. Mitra J, Guerrero EN, Hegde PM, Liachko NF, Wang H, Vasquez V, Gao J, Pandey A, Taylor JP, Kraemer BC, Wu P, Boldogh I, Garruto RM, Mitra S, Rao KS, Hegde ML. Proc Natl Acad Sci USA. 2019; 116:4696. [PubMed: 30770445]

[79]. Tang X, Zhou L, Wagner AM, Marchetto MCN, Muotri AR, Gage FH, Chen G. Stem Cell Res. 2013; 11:743. [PubMed: 23759711]

[80]. Amiri M, Hosseinmardi N, Bahrami F, Janahmadi M. J Comput Neurosci. 2013; 34:489. [PubMed: 23661228]

[81]. Ronchi S, Fiscella M, Marchetti C, Viswam V, Müller J, Frey U, Hierlemann A. Front Neurosci. 2019; 13:208. [PubMed: 30918481]

[82]. Orphanidou C, Bonnici T, Charlton P, Clifton D, Vallance D, Tarassenko L. IEEE J Biomed Health Informatics. 2014; 193:832.

[83]. Pachitariu KD, Steinmetz M, Kadir N, Carandini S, Harris M. BioRxiv. 2016

[84]. Buccino AP, Hurwitz CL, Garcia S, Magland J, Siegle JH, Hurwitz R, Hennig MH. Elife. 2020; 9:e61834. [PubMed: 33170122]

[85]. Hill DN, Mehta SB, Kleinfeld D. J Neurosci. 2011; 31:8699. [PubMed: 21677152]

[86]. Yuan X, Schröter M, Obien MEJ, Fiscella M, Gong W, Kikuchi T, Odawara A, Noji S, Suzuki I, Takahashi J, Hierlemann A, Frey U. Nat Commun. 2020; 11

[87]. Tukker AM, Bouwman LMS, van Kleef RGDM, Hendriks HS, Legler J, Westerink RHS. Sci Rep. 2020; 10

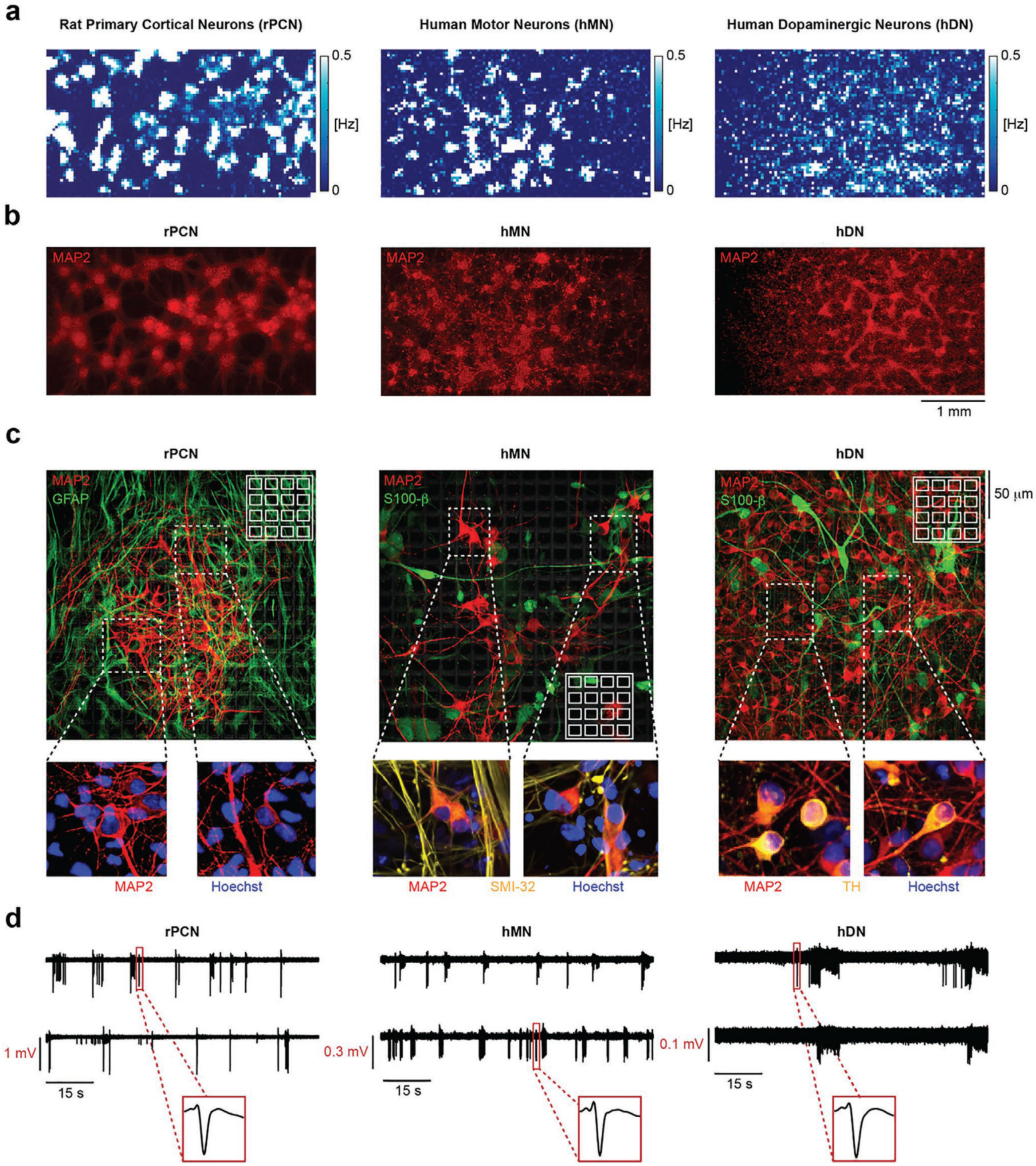

Figure 1. Electrical and optical imaging of neuronal cultures.

a) HD-MEA electrical image showing 2D spatial distribution maps of the electrode firing rate (eFR, see the Experimental Section, HD-MEA Metrics) as recorded across the entire HD-MEA chip surface from 6600 electrodes at DIV 21, for rat primary cortical neurons (rPCNs), human motor neurons (hMNs) and human dopaminergic neurons (hDNs). b) Microscope image of MAP-2 positive (red) stained neurons on HD-MEA chips. Cells were fixed and stained on the HD-MEA chips at DIV 21. c) Cell-type specific stainings of cultures on HD-MEA chips shown in Figure 1b. Cell nuclei are shown in blue (Hoechst positive), motor neurons (SMI-32 positive) and dopaminergic neurons (TH positive) in yellow, astrocytes (GFAP, S100-β positive) in green. White insets with rectangles and grids schematically represent electrode sizes and spacing. d) Example voltage traces showing extracellular action potentials (spikes) recorded by two electrodes at DIV 21. The displayed traces are taken from electrodes recording action potentials with comparably large amplitudes. A close-up of an averaged action potential waveform is displayed in the red rectangles. Left panel: rat primary cortical neurons. Central panel: human motor neurons. Right panel: human dopaminergic neurons.

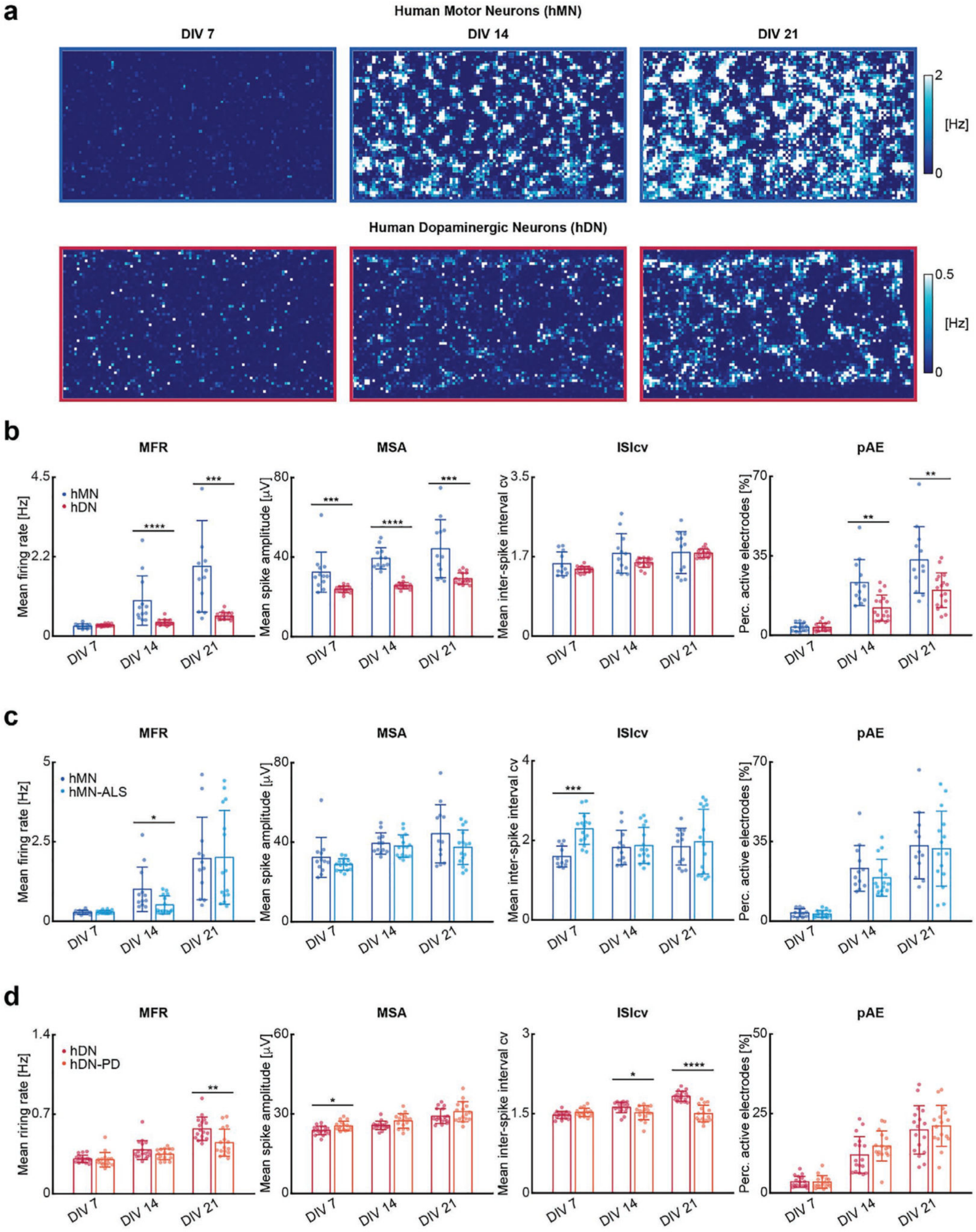

Figure 2. Electrical phenotype characterization of human iPSC-derived neurons across development.

a) Exemplary 2D spatial distribution maps (6600 electrodes) of electrode firing rates for motor neurons (top) and dopaminergic neurons (bottom), at DIVs 7, 14, and 21, respectively. b) Bar plots comparing the mean firing rate (MFR), mean spike amplitude (MSA), mean ISI coefficient of variation (ISIcv) and percentage of active electrodes (pAE) of 12 hMN cultures (blue) and 17 hDN cultures (red) at DIVs 7, 14 and 21. c) Bar plots comparing the mean firing rate, mean spike amplitude, mean ISI coefficient of variation and percentage of active electrodes of 12 hMN cultures (blue) and 15 hMN-ALS cultures (light blue) at DIVs

7, 14, and 21. d) Bar plots comparing the mean firing rate, mean spike amplitude, mean ISI coefficient of variation and percentage of active electrodes of 17 hDN cultures (red) and 16 hDN-PD cultures (orange) at DIVs 7, 14, and 21. Each dot represents one HD-MEA or well. Bar heights indicate distribution mean values, and error bars indicate standard deviations. Pair-wise comparisons were carried out using the two-tailed Wilcoxon rank-sum test. The black stars indicate p values: * $p < 0.05$, ** $p < 0.01$, *** $p < 0.001$, **** $p < 0.0001$.

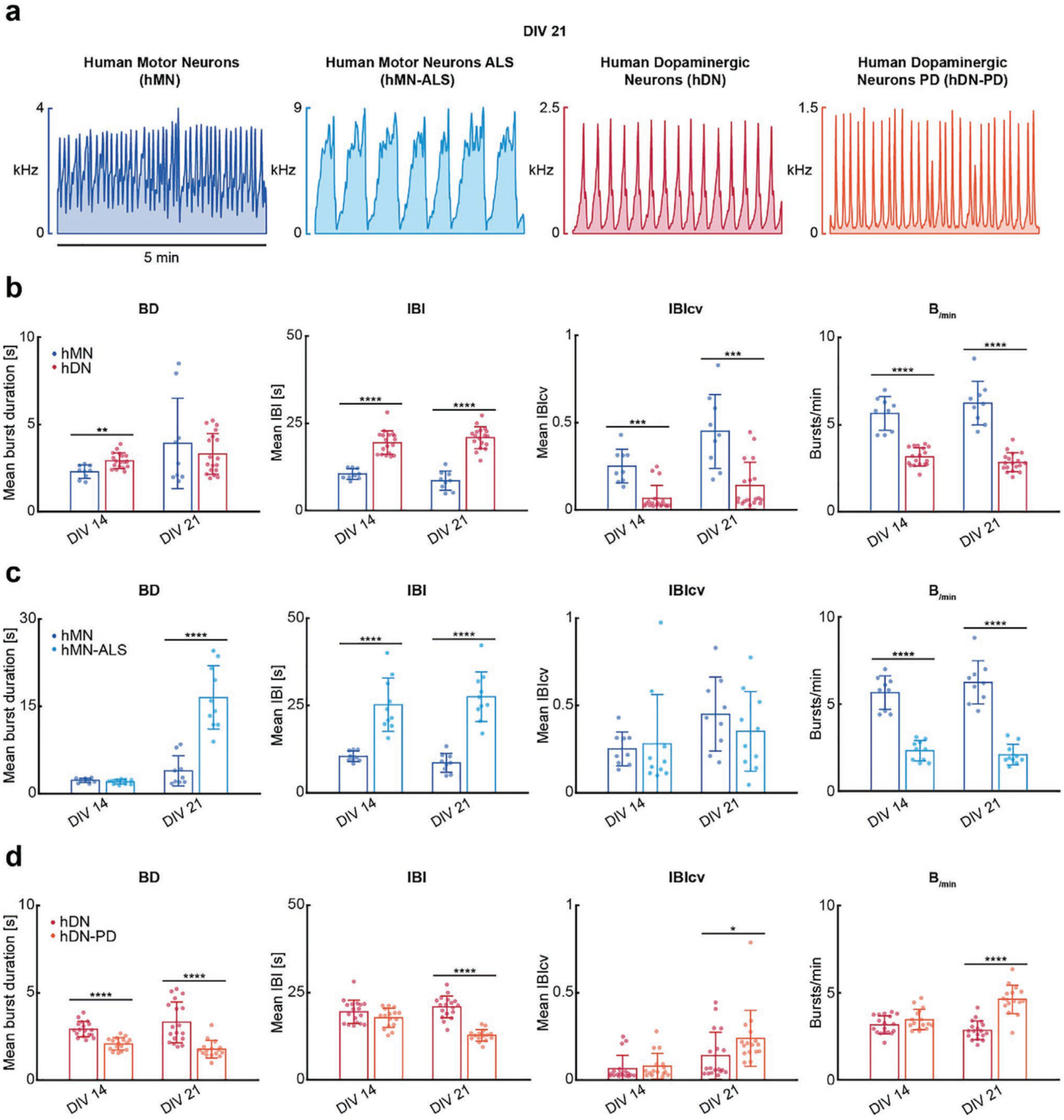

Figure 3. Network burst characterization of human iPSC-derived neurons across development.

a) Population spike time histograms simultaneously recorded by 1024 electrodes from hMN (blue), hMN-ALS (light blue), hDN (red), and hDN-PD (orange) neurons at DIV 21. b) Bar plots comparing mean burst duration (BD), mean inter-burst interval (IBI), mean IBI coefficient of variation (IBIcv) and bursts per min ($B_{/\mathrm{min}}$) of 9 hMN cultures (blue) and 18 hDN cultures (red) at DIVs 14 and DIV 21. Each dot represents one HD-MEA or well. (c) Bar plots comparing mean burst duration, mean IBI, mean IBI coefficient of variation and bursts per min of 9 hMN cultures (blue) and 10 hMN-ALS cultures (light blue) at DIV 14 and DIV 21. Each dot represents one HD-MEA or well. (d) Bar plots comparing mean burst duration, mean IBI, mean IBI coefficient of variation and bursts per min of 18 hDN cultures (red) and 16 hDN-PD cultures (orange) at DIV 14 and DIV 21. Each dot represents one HD-MEA or well. Bar heights indicate distribution mean values, and error bar indicate standard deviations. Pair-wise comparisons were carried out using the two-tailed Wilcoxon rank-sum test. The black stars indicate p values: * $p < 0.05$, ** $p < 0.01$, *** $p < 0.001$, **** $p < 0.0001$.

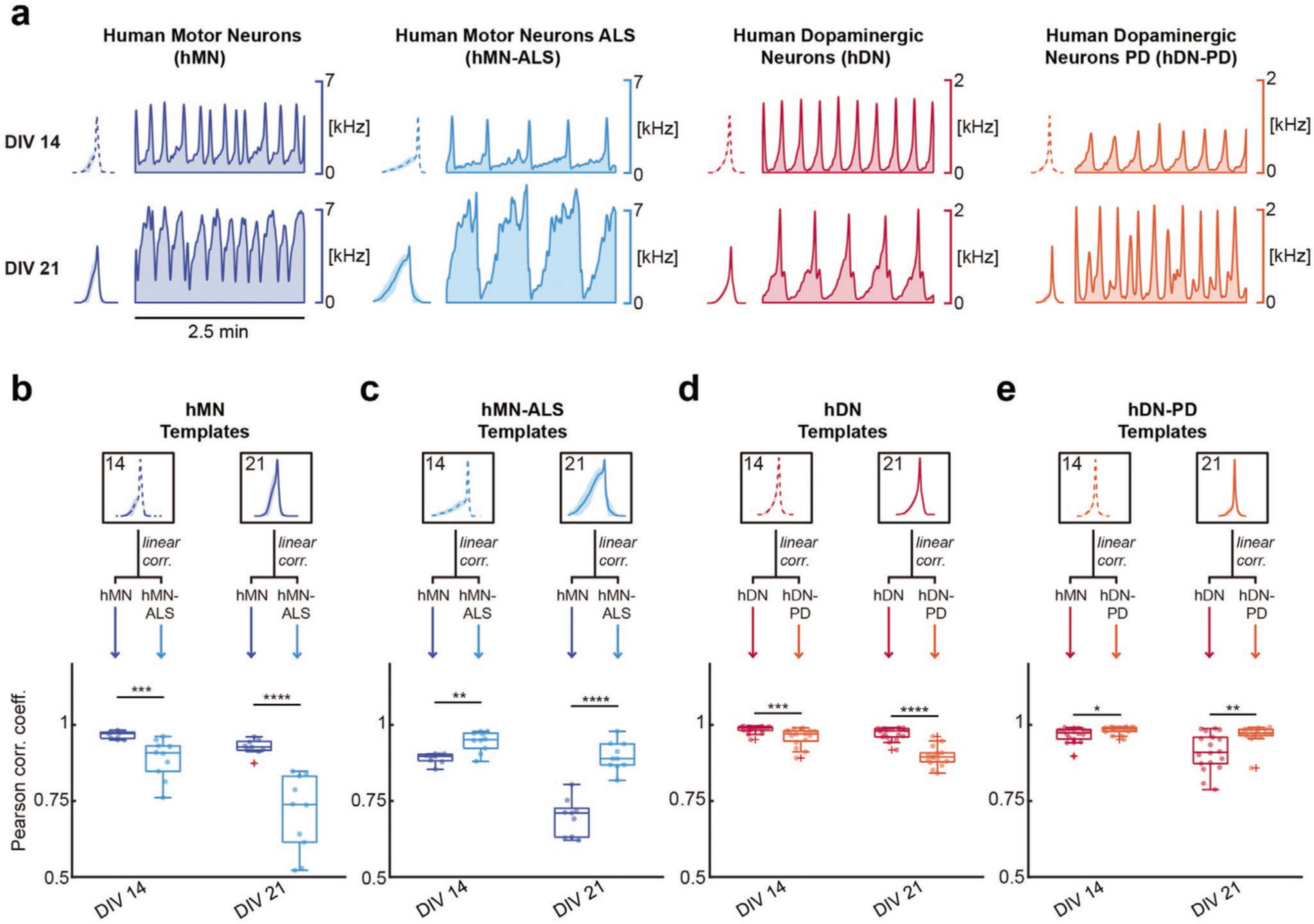

Figure 4. Network burst-shape characterization of human iPSC-derived neurons across development.

a) Population spike time histograms simultaneously recorded by 1024 electrodes from (from left to right) hMN (blue), hMN-ALS (light blue), hDN (red), hDN-PD (orange) neurons at DIV 14 (top) and DIV 21 (bottom). At the left of each panel, an average network burst template is shown for the specific DIV and related neuronal cell type. b) Bar plots comparing the Pearson Correlation Coefficient (PCC) upon linearly correlating the recorded network bursts to the corresponding average templates represented in the top panel. The graph represents the PCC upon linearly correlating burst of healthy motor neurons ($N = 9$) and ALS motor neurons ($N = 10$) to the template obtained from the healthy motor neurons at DIVs 14 and 21. Each dot represents one HD-MEA or well. Box plots indicate distribution mean value and standard deviation. c) PCCs for correlating the hMN-ALS template to bursts of hMN ($N = 9$) and hMN-ALS ($N = 10$) lines. d) PCCs for correlating the hDN template to burst of hDN ($N = 18$) and hDN-PD ($N = 16$) lines. e) PCCs for correlating the hDN-PD template to bursts of hDN ($N = 18$) and hDN-PD ($N = 16$) lines. Pair-wise comparisons were carried out using the two-tailed Wilcoxon rank-sum test. The black stars indicate p values: * $p < 0.05$, ** $p < 0.01$, *** $p < 0.001$, **** $p < 0.0001$.

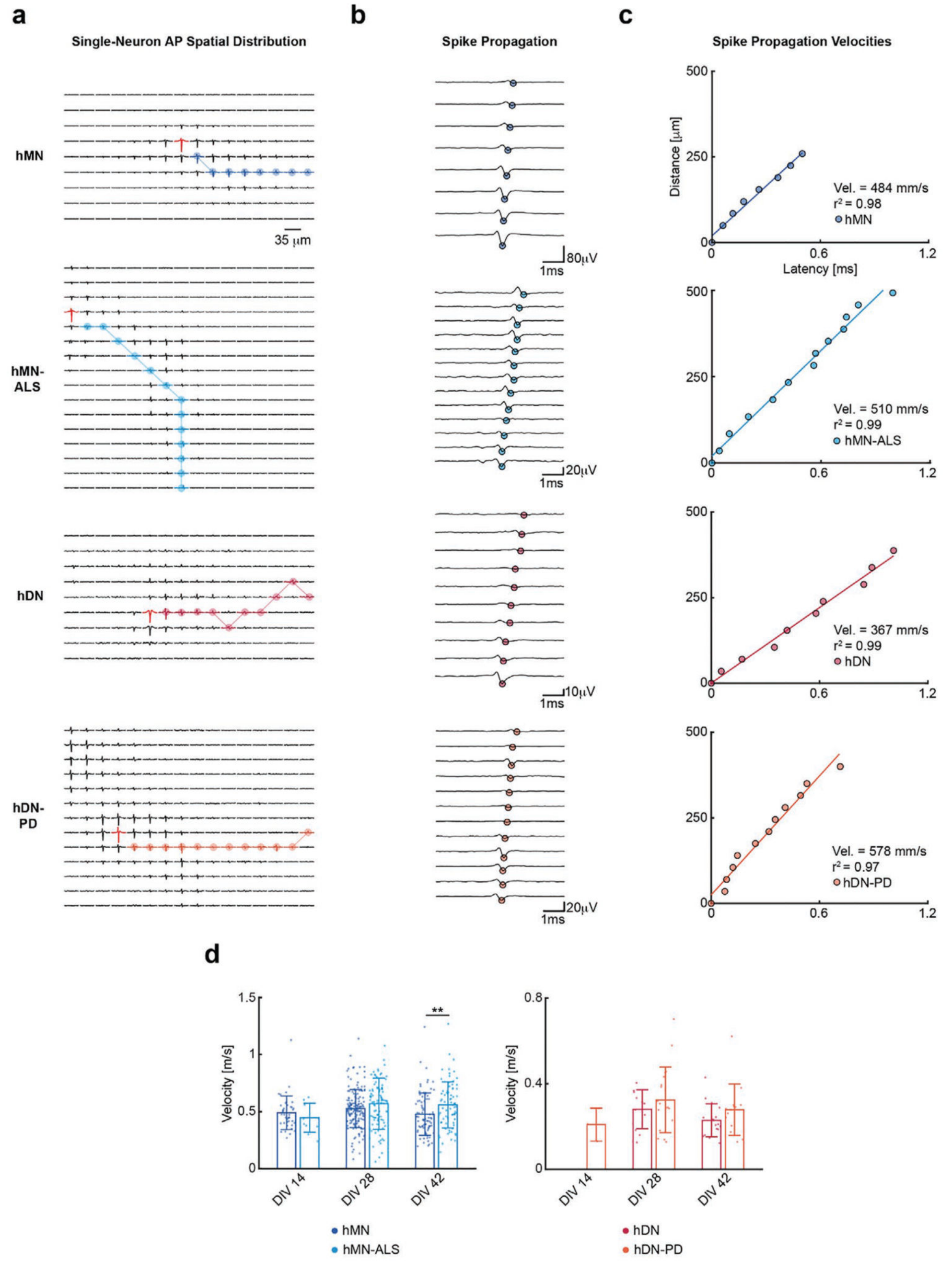

Figure 5. AP propagation velocity computed for different human iPSC-derived neuron lines.

a) Spatial distribution of action potential (AP) waveforms of sample neurons of (top to bottom) hMN, hMN-ALS, hDN, hDN-PD neuronal lines. Each trace represents a cutout of 6 ms of extracellular voltage signal recorded on the respective electrode at DIV 28. The red traces indicate the waveforms on the electrode featuring the largest signal amplitude. The plots are also displayed in Figure S3 at larger magnification. b) AP propagation in time and space, after temporal alignment of the signals of selected readout electrodes represented in (a). Points indicate the voltage minima of the recorded traces. The traces are ordered with respect to delay from top to bottom with the top trace featuring the longest delay and coming from the electrode that is most distant to the axonal initial segment (AIS). c) Linear regression interpolation to compute the AP propagation velocity for the neurons represented in (a) and (b). d) Bar plots comparing the AP propagation velocity of (left) healthy motor neurons and ALS motor neurons and of (right) healthy and PD dopaminergic neurons, at DIVs 14, 28 and 42. Each dot represents one HD-MEA or well. Bar heights indicate distribution mean values, and error bars indicate standard deviations. Pair-wise comparisons were carried out using the two-tailed Wilcoxon rank-sum test. The stars indicate p values: ** $p < 0.01$. The number (N) of hMNs for which velocities were determined at DIVs 14, 28 and 42 is 40, 165 and 80, respectively. The number (N) of hMN-ALSs for which velocities were determined at DIV 14, 28 and 42 is 11, 92 and 76, respectively. The number (N) of hDNs for which velocities were determined at DIVs 28 and 42 is 11 and 17, respectively. The number (N) of hDN-PDs for which velocities were determined at DIVs 14, 28, and 42 is 3, 19, and 14, respectively.

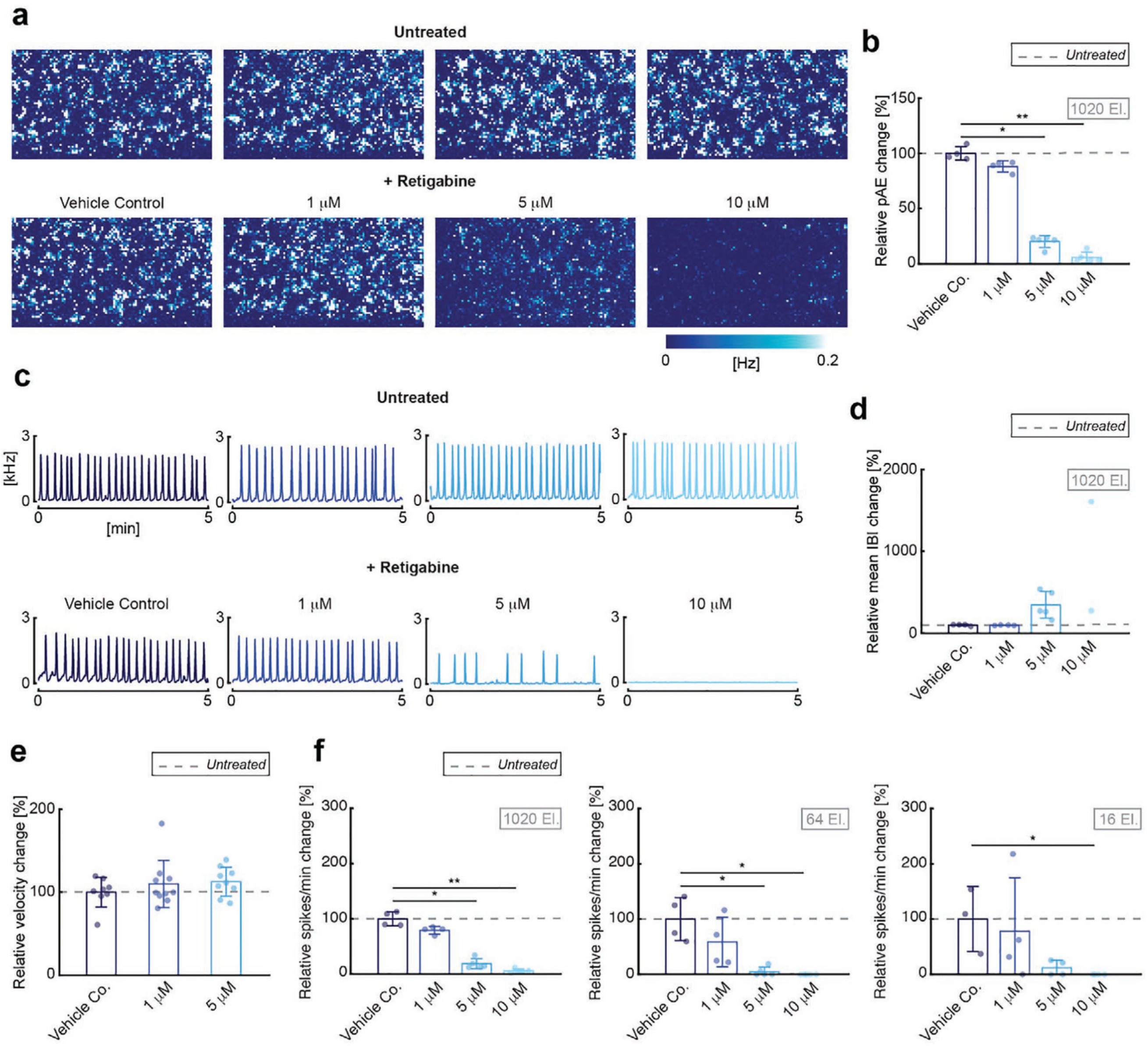

Figure 6. Retigabine effect on motor neurons on spikes per m, IBI and active electrodes.

a) 2D spatial distribution maps of electrode spike rates recorded from four exemplary HD-MEAs at DIV 14. Signals from 6600 electrodes per HD-MEA were recorded before drug administration (top row) and one minute after drug administration (bottom row) for different retigabine concentrations. b) Bar plots representing the relative change (percent) in active electrodes for each applied retigabine concentration and for the vehicle control with respect to pre-treatment conditions. Each dot represents one HD-MEA or well. Bar heights indicate distribution mean values and error bars indicate standard deviations. The dashed gray line marks the values (100%) before drug treatment. The number of HD-MEAs or wells included $N = 4$ for vehicle control and 1 µm retigabine concentration and $N = 5$ for 5 µm and 10 µm retigabine concentrations. c) Population spike time histograms of four representative HD-

MEAs, recorded before (top row) and after drug administration (bottom row) for different retigabine concentrations. d) Bar plots representing the relative change in the mean IBI for each applied retigabine concentration and for the vehicle control, normalized to pre-treatment conditions. e) Bar plots representing the relative change in axonal velocity upon exposure to the vehicle control ($N = 8$ neurons), 1 µm of retigabine ($N = 10$ neurons) and 5 µm of retigabine ($N = 9$ neurons), normalized to pre-treatment conditions. f) Spikes per min-values computed as relative change with respect to the situation before drug administration. Plots show spikes per min-values for using signals from the 1020 most active electrodes at a minimum pitch of 35, µm selected from the overall array of 26 400 electrodes (left), and configurations of 64 electrodes (center) and 16 electrodes at 200 µm pitch (right). For more details, see also Figure S5a. To compare multiple groups, we used the Kruskal-Wallis test, followed by the Dunn-Sidák multiple-comparison test. The individual pair-wise test was conducted at the Sidák-corrected α value of 0.017. The black stars indicate p values with respect to vehicle control: * $p < 0.017$, ** $p < 0.001$.

Table 1

Antibodies. The table describes primary and secondary antibodies used in this work.

Antibody	Supplier	Ratio	Binds to	Catalogue #
Anti MAP2	EnCor	1:500	Microtubules	CPCA-MAP2
Anti TH	Pel Freeze	1:1000	Tyrosine hydroxylase enzyme	P60101-150
Anti GFAP	Abcam	1:500	GFAP	Ab7260
Anti S-100	Abcam	1:200	Zn	Ab52642
Anti Smi-32	Abcam	1:500	Neurofilaments	Ab7795
Hoechst	Thermofisher Scientific	1:500	DNA	H3570